The Astrophysical Journal Letters, 980:L27 (8pp), 2025 February 20 https://doi.org/10.3847/2041-8213/adaebd

Extremely Dense Gas around Little Red Dots and High-redshift Active Galactic Nuclei: A Nonstellar Origin of the Balmer Break and Absorption Features

Kohei Inayoshi[1] and Roberto Maiolino[2,3,4]
[1] Kavli Institute for Astronomy and Astrophysics, Peking University, Beijing 100871, People's Republic of China; inayoshi@pku.edu.cn
[2] Kavli Institute for Cosmology, University of Cambridge, Madingley Road, Cambridge, CB3 OHA, UK
[3] Cavendish Laboratory—Astrophysics Group, University of Cambridge, 19 JJ Thomson Avenue, Cambridge, CB3 OHE, UK
[4] Department of Physics and Astronomy, University College London, Gower Street, London WC1E 6BT, UK
Received 2024 September 18; revised 2025 January 11; accepted 2025 January 23; published 2025 February 13

Abstract

The James Webb Space Telescope (JWST) has uncovered low-luminosity active galactic nuclei (AGNs) at high redshifts of $z \gtrsim 4$–7, powered by accreting black holes with masses of $\sim 10^{6-8}\,M_\odot$. One remarkable distinction of these JWST-identified AGNs, compared to their low-redshift counterparts, is that at least ∼20% of them present Hα and/or Hβ absorption, which must be associated with extremely dense ($\gtrsim 10^9\,\mathrm{cm}^{-3}$) gas in the broad-line region or its immediate surroundings. These Balmer absorption features unavoidably imply the presence of a Balmer break caused by the same dense gas. In this Letter, we quantitatively demonstrate that a Balmer break can form in AGN spectra without stellar components, when the accretion disk is heavily embedded in dense neutral gas clumps with densities of $\sim 10^{9-11}\,\mathrm{cm}^{-3}$, where hydrogen atoms are collisionally excited to the $n = 2$ states and effectively absorb the AGN continuum at the bluer side of the Balmer limit. The nonstellar origin of a Balmer break offers a potential solution to the large stellar masses and densities inferred for little red dots (LRDs) when assuming that their continuum is primarily due to stellar light. Our calculations indicate that the observed Balmer absorption blueshifted by a few hundred $\mathrm{km\,s}^{-1}$, which suggests the presence of dense outflows in the nucleus at rates exceeding the Eddington value. Other spectral features such as higher equivalent widths of broad Hα emission and presence of O I lines observed in high-redshift AGNs including LRDs align with the predicted signatures of a dense super-Eddington accretion disk.

Unified Astronomy Thesaurus concepts: Galaxy formation (595); High-redshift galaxies (734); Quasars (1319); Supermassive black holes (1663)

1. Introduction

The James Webb Space Telescope (JWST) is rapidly advancing our exploration of the high-redshift universe. With its exceptional sensitivity, JWST has uncovered numerous intermediate/low-luminosity active galactic nuclei (AGNs), enabling us to study the representative population of accreting black holes (BHs) at cosmic dawn (e.g., Y. Harikane et al. 2023; D. D. Kocevski et al. 2023; R. Maiolino et al. 2024, 2024b; M. Onoue et al. 2023).

Among the most intriguing discoveries are very compact, red-colored sources with broad-emission-line (FWHM $\gtrsim 1500\,\mathrm{km\,s}^{-1}$) features in their spectra (e.g., G. Barro et al. 2024; J. E. Greene et al. 2024; I. Labbe et al. 2023; J. Matthee et al. 2024). These so-called "little red dots" (LRDs) are considered to be dust-reddened AGNs at $z \sim 4$–8, with bolometric luminosities of $L_{\rm bol} \sim 10^{44-47}\,\mathrm{erg\,s}^{-1}$ powered by massive BHs with $10^{7-8}\,M_\odot$, if dust attenuation correction derived from the red continua in the rest-frame optical bands is applied. Remarkably, the cosmic abundance of these LRDs is 1 order (or 2 orders, if the whole AGN population is considered) of magnitude higher than what was expected from previous quasar surveys (H. B. Akins et al. 2024; V. Kokorev et al. 2024a; D. D. Kocevski et al. 2024). If all these bright LRDs are AGNs, this would imply that the radiative efficiency is approaching the theoretical limit, requiring a potential reevaluation of current observations or theoretical models (K. Inayoshi & K. Ichikawa 2024).

Despite their significance, the properties of the newly identified LRDs remain puzzling, particularly regarding the origin of their characteristic v-shaped spectral energy distribution (SED) in the rest-frame UV-to-optical bands (I. Labbe et al. 2023; J. E. Greene et al. 2024; B. Wang et al. 2024a). Possible explanations for this feature include contributions from galaxies, AGNs, or a combination of both. Recently, deep spectroscopic observations have revealed a prominent drop near the Balmer limit in the continuum spectra of some LRDs (J. F. W. Baggen et al. 2024; L. J. Furtak et al. 2024; J. E. Greene et al. 2024; V. Kokorev et al. 2024b B. Wang et al. 2024a, 2024b), suggesting a potential contribution from the host galaxy stellar light. This finding is crucial for understanding the energy source of LRDs. If LRDs are powered by dusty starburst galaxies alone, the inferred stellar mass would exceed a few times $10^{10}\,M_\odot$ and in some cases reach up to $\sim 10^{11}\,M_\odot$, which would conflict with the standard structure formation framework if such huge masses were formed at $z \gtrsim 7$ (B. Wang et al. 2024b; H. B. Akins et al. 2024; K. Inayoshi & K. Ichikawa 2024). Additionally, when combined with the extremely compact sizes, the stellar densities would be so high that velocity dispersions could reach $\gtrsim 1000\,\mathrm{km\,s}^{-1}$, a phenomenon never observed in local or lower-redshift galaxies (J. F. W. Baggen et al. 2024; also P. F. Hopkins et al. 2010). Alternatively, if the light redward of the Balmer break originates from a nonstellar source (with stellar light dominating only at shorter wavelengths), the inferred stellar mass could be significantly lowered on the order of $\sim 10^9\,M_\odot$, aligning with structure formation models. However, this scenario would still need an AGN contribution at longer wavelengths to explain the continuum with a steep red color and broad Balmer emission lines. Another interpretation suggests that the UV component of

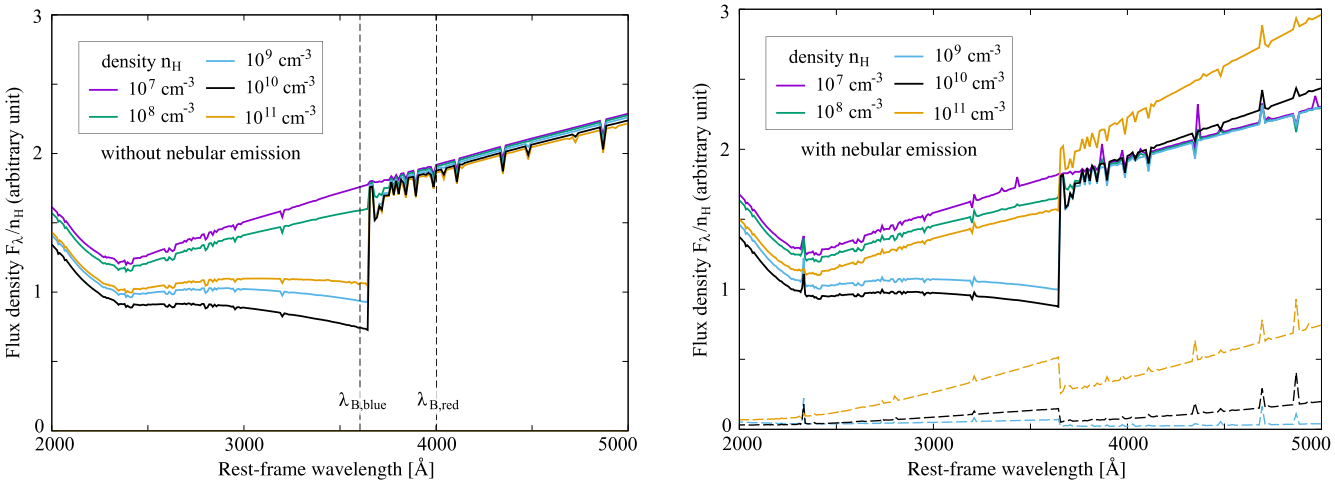

Figure 1. Left: AGN SEDs attenuated through a gas slab with a visual extinction of $A_V = 3$ mag with $Z = 0.1\,Z_\odot$. Each curve represents the case with different density ($10^7 \leqslant n_H/\mathrm{cm}^{-3} \leqslant 10^{11}$) and thickness. With high densities of $n_H \simeq 10^{9-11}$ cm^{-3}, the SEDs show a deep Balmer break at $\lambda_{B,lim} = 3646$ Å. Two vertical lines indicate the wavelengths ($\lambda_{B,blue} = 3600$ Å and $\lambda_{B,red} = 4000$ Å) used to quantify the Balmer break strength. Right: total AGN SEDs, including the nebular emission with a covering fraction of $C = 0.5$. For the cases with $n_H = 10^{9-11}$ cm^{-3}, the nebular components are shown separately (dashed). The Balmer jump feature of the nebular spectrum weakens the Balmer break strength in the total SED when dense absorbers with $n_H \gtrsim 10^{11}$ cm^{-3} surround the AGN with a high covering fraction ($C \gtrsim 0.5$).

the SED could be influenced by a gray dust attenuation curve, resulting from the deficit of small-size dust grains, which might explain the v-shaped SED of LRDs (Z. Li et al. 2025).

Moreover, an independent line of evidence comes from the detailed analysis of broad hydrogen emission lines in AGNs observed by JWST, not only in LRDs but also in unobscured sources (R. Maiolino et al. 2024; I. Juodžbalis et al. 2024; D. D. Kocevski et al. 2024; X. Lin et al. 2024; J. Matthee et al. 2024). These observations reveal slightly blueshifted and narrow absorption on the broad Balmer lines ($v \simeq 200\,\mathrm{km\,s^{-1}}$). The detection of H$\alpha$ and Hβ in absorption is remarkable as the $n = 2$ states of atomic hydrogen are very short-lived and not metastable. To make such absorption features visible against the Balmer emission profile, extremely high gas densities are required to populate hydrogen atoms into the $n = 2$ states. In particular, I. Juodžbalis et al. (2024) infer that Hα and Hβ absorption must be associated with very dense gas along the line of sight with $n_H > 10^9\,\mathrm{cm}^{-3}$, possibly clouds of the broad-line region (BLR) or its immediate surroundings. In nearby AGNs, Balmer absorption lines are rarely observed with a detection rate of ≈0.1%. However, Balmer absorption has been found in at least 10%–20% of broad-line AGNs observed by JWST (see Figure 12 of X. Lin et al. 2024). Since higher-resolution spectroscopy is required to detect these absorption lines, the fraction of 10%–20% is likely a lower limit, and thus a larger fraction of AGNs are probably buried in dense gas distributed over a wide solid angle.

In this Letter, we demonstrate that a Balmer break feature can form in AGN spectra without stellar components when the accretion disk is heavily embedded in dense neutral gas clumps with densities of $\simeq 10^{9-11}\,\mathrm{cm}^{-3}$, where hydrogen atoms are collisionally excited to the $n = 2$ states and effectively absorb the AGN continuum at the bluer side of the Balmer limit. Under these circumstances, the dense gas clump naturally leads to deep absorption on top of the broad Balmer emission lines, as observed in JWST AGNs. We further discuss the physical mechanism of launching dense outflows imprinted in the blueshifted Balmer absorption and other spectral features of accreting BHs embedded in dense environments.

2. Balmer Break

To quantify the SED shape of an attenuated incident flux from the galactic nucleus, we make use of CLOUDY (C17, G. J. Ferland et al. 2017) to perform line transfer calculations along with hydrogen level population modeling simultaneously. In our model, the incident radiation source is an AGN (an accretion disk and nonthermal radiation), and its spectral shape is assumed to be

$$f_\nu \propto \max[\nu^{\alpha_{uv}} e^{-h\nu/k_B T_{bb}},\quad r_x \nu^{\alpha_x}], \tag{1}$$

where we set the temperature of the big blue bump to $T_{bb} = 10^5$ K,[5] the UV and X-ray spectral indices to $\alpha_{uv} = -0.5$ and $\alpha_x = -1.5$, and the normalization of r_x is adjusted so that the spectral slope between 2500 Å and 2 keV becomes $\alpha_{ox} = -1.5$. The value of $\alpha_{uv} = -0.5$ is consistent with that of the low-redshift composite quasar SED (D. E. Vanden Berk et al. 2001). The X-ray spectral index would be steeper, as observed in bright quasars at high redshifts ($\alpha_x \lesssim -2$; L. Zappacosta et al. 2023); however, our results are unaffected by the specific value of the index. The flux density normalization is determined such that the ionization parameter, $U \equiv \Phi_0/(n_H c)$, falls within $-2 \leqslant \log U \leqslant -1$, where Φ_0 is the ionizing photon number flux, n_H is the number density of hydrogen nuclei, and c is the speed of light. In this study, we adopt $\log U = -1.5$ as the fiducial choice. Note that the Balmer break strength varies by ≃10%–20% depending on the ionization parameter within the range. The distance of the gas absorber derived using $\log U = -1.5$ is consistent with the cloud kinematics, as discussed in Section 4.1. We consider a plane-parallel geometry of the absorber assuming that individual clouds have a small cross section. Then, the total SED is calculated by combining the transmitted and nebular components, with the nebular contribution scaled by a covering fraction C for gas absorbers within the

[5] The characteristic temperature corresponds to the value measured at $r \sim 10\,r_g$ in an accretion disk around a BH with $M_\bullet = 10^{7-8}\,M_\odot$ accreting at the Eddington rate, where r_g is the Schwarzschild radius. Note that the surface temperature profile saturates within $10\,r_g$ and declines toward the innermost stable circular orbit, where the torque-free boundary conditions are imposed (I. D. Novikov & K. S. Thorne 1973).

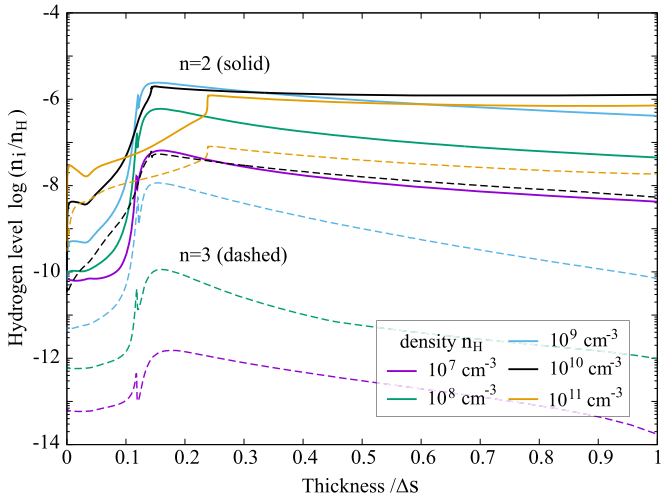

Figure 2. Profiles of the hydrogen level populations in the $n = 2$ (solid) and $n = 3$ (dashed) states as a function of slab thickness normalized by the total value Δs for each density case; $n_H = 10^7 - 10^{11}$ cm^{-3}. The values are normalized by the total density of hydrogen nuclei (n_H), including both neutral and ionized states. As the density increases, the hydrogen is excited to the higher-energy states. The ratio of $n = 2$ states reaches $n_2/n_H \simeq 10^{-6}$, which is the equilibrium value with $T \simeq 8000$ K through particle collisions.

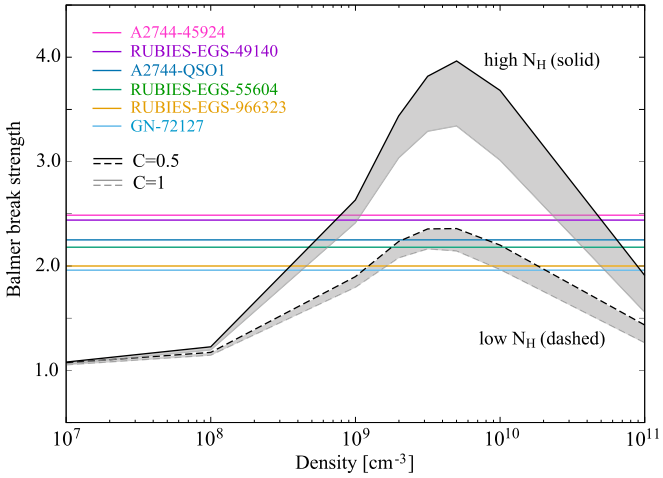

Figure 3. The Balmer break strength defined by $F_\lambda(\lambda_{B,red})/F_\lambda(\lambda_{B,blue})$ for $N_H = 5.4 \times 10^{22}$ (dashed) and 1.7×10^{23} cm^{-2} (solid). Two covering fractions are considered: $C = 0.5$ (black) and $C = 1$ (gray). For the fiducial case (black and dashed curve), the Balmer break strength reaches values of $\geqslant 2$ in the density range of $10^9 \lesssim n_H/\mathrm{cm}^{-3} \lesssim 2 \times 10^{10}$. With increasing column density, the Balmer break becomes more prominent due to the enhanced column density of atomic hydrogen in the $n = 2$ state. These depths are consistent with those of six broad-line LRDs that show a Balmer break in the PRISM spectrum (L. J. Furtak et al. 2024; B. Wang et al. 2024b; V. Kokorev et al. 2024b; I. Labbe et al. 2024; see the text).

hemisphere facing the observer. For the fiducial model, we assume a visual extinction of $A_V = 3$ mag to match the redness observed in the rest-optical continua for LRDs (J. Matthee et al. 2024; J. E. Greene et al. 2024). With a metallicity of $0.1\,Z_\odot$, the column density is approximated to $N_H \simeq 5.4 \times 10^{22}\,\mathrm{cm}^{-2}(Z/0.1\,Z_\odot)^{-1}$. We vary the gas density over a broad range of $10^7 \leqslant n_H/\mathrm{cm}^{-3} \leqslant 10^{11}$, adjusting the slab thickness (Δs) to maintain a fixed visual extinction. In this analysis, we do not account for the effects of microscopic turbulence, whose influence on the SED shape will be studied in a forthcoming paper (X. Ji et al. 2025).

The left panel of Figure 1 presents the SEDs of an attenuated AGN for various densities of $10^7 \leqslant n_H/\mathrm{cm}^{-3} \leqslant 10^{11}$. When the density is $n_H = 10^7\,\mathrm{cm}^{-3}$ or lower, the SED maintains a smooth red continuum at $\lambda \gtrsim 2500$ Å and a slightly blue one at the shorter wavelengths. The bending of the SED at $\lambda \simeq 2500$ Å is attributed to the gray dust attenuation curve, though variations in the curve model can lead to different results (Z. Li et al. 2025), which we do not explore in detail here. As the density increases to $n_H = 10^8\,\mathrm{cm}^{-3}$, the continuum component at wavelengths shorter than the Balmer limit ($\lambda_{B,lim} = 3646$ Å) becomes steeper, and the discontinuity across the Balmer limit reaches its peak around $n_H = 10^{9-10}\,\mathrm{cm}^{-3}$. However, as the density further increases to $\simeq 10^{11}\,\mathrm{cm}^{-3}$, the discontinuity weakens but converges in the higher-density regime.

The right panel of Figure 1 shows the total AGN SEDs (solid) including the nebular emission with a covering fraction of $C = 0.5$. For demonstration, the cases of $n_H = 10^{9-11}\,\mathrm{cm}^{-3}$ are presented with the nebular components separately (dashed). For $n_H = 10^{9-10}\,\mathrm{cm}^{-3}$, the Balmer break imprinted by dense gas absorbers remains prominent. However, at higher densities ($n_H \gtrsim 10^{11}\,\mathrm{cm}^{-3}$) and a high covering fraction ($C \gtrsim 0.5$), the Balmer jump feature in the nebular emission reduces the apparent strength of the Balmer break in the total SED.

Figure 2 shows the number-density ratio of atomic hydrogen in excited states ($n = 2$ with solid and $n = 3$ with dashed curves) to the total density of hydrogen nuclei including neutral and ionized states as a function of slab thickness. At low densities ($n_H \lesssim 10^8\,\mathrm{cm}^{-3}$), the number ratios of excited states in both $n = 2$ and $n = 3$ increase proportionally with the density, indicating that atomic hydrogen has not reached a local thermodynamic equilibrium state for a given temperature. However, as the density reaches $n_H \simeq 10^9\,\mathrm{cm}^{-3}$, the ratio of $n = 2$ states begins to saturate, approaching the collisional equilibrium value of $n_2/n_H \simeq 10^{-6}$ for $T \simeq 8000$ K. When the density further increases to $n_H = 10^{10}\,\mathrm{cm}^{-3}$, the ratio of the $n = 3$ state atomic hydrogen also starts to saturate. The Balmer break strength is closely linked to the population of hydrogen in the $n = 2$ state. Effective collisional pumping to the $n = 2$ state leads to significant attenuation of AGN flux at wavelengths just blueward of the Balmer limit, naturally producing a Balmer break. This process is analogous to the Lyman break, which results from neutral atomic hydrogen in the ground state ($n = 1$) absorbing ionizing radiation.

Figure 3 presents the Balmer break strength of the total AGN SEDs as a function of slab density. We measure the Balmer break strength using the ratio of the fluxes on the blue ($\lambda_{B,blue}$) and red sides ($\lambda_{B,red}$) of the Balmer limit. To compare our result with LRDs that show both broad Balmer lines and a Balmer break in the spectra reported by B. Wang et al. (2024b), we adopt $\lambda_{B,blue} = 3600$ Å and $\lambda_{B,red} = 4000$ Å. We here show cases for two different column densities: $N_H = 5.4 \times 10^{22}\,\mathrm{cm}^{-2}$ (dashed; fiducial model) and $1.7 \times 10^{23}\,\mathrm{cm}^{-2}$ (solid). These column densities are adjusted to maintain $A_V = 3$ mag, which thus corresponds to metallicities of 10^{-1} and $10^{-1.5}\,Z_\odot$, respectively. For the fiducial case ($N_H = 5.4 \times 10^{22}\,\mathrm{cm}^{-2}$), the Balmer break strength reaches values of $\geqslant 2$ in the density range of $10^9 \lesssim n_H/\mathrm{cm}^{-3} \lesssim 2 \times 10^{10}$. With increasing column density, the Balmer break becomes more prominent due to the enhanced column density of atomic hydrogen in the $n = 2$ state. The density range with a Balmer break strength $\geqslant 2$ is extended to $3 \times 10^8 \lesssim n_H/\mathrm{cm}^{-3} \lesssim 10^{11}$ for the case of $N_H = 1.7 \times 10^{23}\,\mathrm{cm}^{-2}$. These trends hold even when the higher covering fraction is set ($C = 1$; gray curves), though these cases show slightly weaker Balmer break depths compared to those with

$C = 0.5$ (black curves). The measured strengths are consistent with observations of RUBIES-EGS-49140, 55604, and 966323 (B. Wang et al. 2024b), A2744-QSO 1 (L. J. Furtak et al. 2024), GN-72127 (V. Kokorev et al. 2024b), and A2744-45924 (I. Labbe et al. 2024). At the high-density limit of $n_{\rm H} \gg 10^{10}\,{\rm cm}^{-3}$, the Balmer break strength weakens due to the contributions of the Balmer jump from the nebular emission.

A sufficiently high hydrogen column density, likely attributed to dense absorbers such as clouds in the BLR or its surroundings, is required to imprint a Balmer break on the AGN SED. While BLR clouds, or more generally clouds located within the conventional sublimation radius, are typically considered dust free, large dust grains ($a \gtrsim 0.06\,\mu$m) in dense clouds with $n_{\rm H} \gtrsim 10^{9-10}\,{\rm cm}^{-3}$ may survive even at BLR scales ($\sim 2R_{\rm BLR}$) due to the effective thermal energy loss from their surfaces (A. Baskin & A. Laor 2018). These grains are thermally decoupled from the surrounding hot gas (e.g., K. E. I. Tanaka & K. Omukai 2014) and maintain their temperature below the sublimation threshold (i.e., $T_{\rm dust} < T_{\rm sub} \ll T$) when

$$\frac{n_{\rm H}}{10^{15}\quad {\rm cm}^{-3}} < 2.4\left(\frac{T_{\rm dust}}{10^3\quad {\rm K}}\right)^4\left(\frac{T}{10^4\quad {\rm K}}\right)^{-3/2}, \tag{2}$$

where the dust Planck mean opacity is approximately constant for $100\,{\rm K} \lesssim T_{\rm dust} \lesssim T_{\rm sub}$. As a result, dust grains can survive in dense absorbers with $n_{\rm H} \lesssim 10^{9-11}\,{\rm cm}^{-3}$, where the AGN SED exhibits a prominent Balmer break feature under a high column density of $N_{\rm H} \sim 10^{23}\,{\rm cm}^{-2}$. Assuming the depletion factor of metals onto dust grains is comparable to the present-day galactic value ($f_{\rm dep} \sim 0.5$), the metallicity needs to be as low as $Z \sim 10^{-1.3}\,Z_\odot$ to maintain $A_V \sim 3$ mag. At higher metallicities ($Z \gtrsim 10^{-0.5}\,Z_\odot$), unless the depletion factor is significantly lower, the visual extinction could become so large that the AGN emission is severely obscured ($A_V \gtrsim 20$). In such cases, these systems would likely be observed as Type II AGNs.

Intriguingly, dense absorbers containing large-size grains ($a_{\rm min} \sim 0.06\quad \mu$m) yield a gray extinction curve at wavelengths shorter than $\lambda \simeq 2\pi a_{\rm min} \simeq 3800$ Å. This characteristic may help explain the v-shaped SEDs observed in LRDs, which consist of a red optical continuum and a UV excess with a turnover wavelength near the Balmer limit (see the discussion in Z. Li et al. 2025). Further studies of dust sublimation and (re) formation mechanisms in dense BLR clouds will be crucial to understanding the properties of high-redshift AGNs identified through JWST observations.

3. Balmer Absorption

In this section, we examine how Hα absorption modulates the line profile under the conditions that satisfy the criteria for producing a Balmer break, as discussed in Section 2. The optical depth of a bound–bound transition between two (upper u and lower ℓ) energy states of atomic hydrogen is given by

$$\tau_0 \approx \frac{\sqrt{\pi}e^2}{m_{\rm e}c}\frac{f_{\ell u}\lambda_{\ell u}N_{{\rm H}\ell}}{b} = 314\quad N_{{\rm H}\ell,16}b_{200}^{-1}, \tag{3}$$

(B. T. Draine 2011), where e is the elementary charge, $m_{\rm e}$ the electron mass, $f_{\ell u}$ the oscillation strength between the two states, and $\lambda_{\ell u}$ the wavelength of a photon emitted in the transition. For Hα ($u = 3$ and $\ell = 2$), $f_{\ell u} = 0.6047$ and $\lambda_{\ell u} = 6563$ Å$(= \lambda_0)$ (e.g., H. W. Drawin 1969). The optical depth at a frequency ν near the line center ν_0 is approximated as $\tau_\nu = \tau_0 e^{-(u/b)^2}$, with $u = c(1 - \nu/\nu_0)$ and $b = \sqrt{2}\,\sigma_v$, where σ_v is the one-dimensional velocity dispersion. Following I. Juodžbalis et al. (2024), the absorption feature at a wavelength λ is modeled using the attenuation formula

$$f_\lambda = 1 - C + Ce^{-\tau_\lambda}, \tag{4}$$

where

$$\tau_\lambda = \tau_0 \exp\left[-\frac{(\Delta v - c\lambda/\lambda_0)^2}{b^2}\right], \tag{5}$$

with Δv representing the velocity shift, where a negative value indicates a blueshift.

We apply the attenuation feature to the broad-line component of the Hα emission while excluding the narrow-line component. This approach is based the idea that dense gas clumps are located between the BLRs and narrow-line regions (see also Section 4.1) and thus absorb only the broad-line emission component. The Hα line profile is modeled as

$$F_\lambda = \phi_\lambda(\lambda_0, \sigma_{\rm broad})f_\lambda + r\phi_\lambda(\lambda_0, \sigma_{\rm narrow}), \tag{6}$$

where $\phi_\lambda(\lambda_0, \sigma)$ is a Gaussian function with a mean λ_0 and dispersion σ. The parameters $\sigma_{\rm broad}$ and $\sigma_{\rm narrow}$ represent the one-dimensional velocity dispersion for the broad and narrow components, respectively, and r is the relative ratio between the narrow and broad components before accounting for absorption. In this analysis, we do not consider the continuum flux, for which the same level of attenuation should be applied. In this case, the apparent absorption feature becomes deeper as the unattenuated flux is higher, i.e., $\Delta F_\lambda \propto F_{\lambda,{\rm broad+cont}}$.

In Figure 4, we present the Hα line profile with ${\rm FWHM}_{\rm broad} = 3000\,{\rm km\,s}^{-1}$, ${\rm FWHM}_{\rm narrow} = 400\,{\rm km\,s}^{-1}$, and $r = 0.3$. The choice of the FWHM values aligns with the average ones for broad Hα emission of LRD samples in J. Matthee et al. (2024). We explore two cases: (1) $b = 150\,{\rm km\,s}^{-1}$, $\Delta v = -200\,{\rm km\,s}^{-1}$, and $C = 0.5$ and (2) $b = 10\,{\rm km\,s}^{-1}$, $\Delta v = +50\,{\rm km\,s}^{-1}$, and $C = 0.8$. In the first case, the broad emission line shows a saturated, box-shaped absorption profile. Due to the blueshift of the absorption line center, the absorption appears just to the blue side of the line center when combined with the narrow emission line component. In the second case, the absorption depth is more profound because of the narrower absorption width and larger covering fraction. Since the absorption is slightly redshifted, the absorption features are present on top of the narrow-line emission profile. Those profiles resemble the spectral shapes seen in GOODS-N-9771 and J1148-18404, two LRD samples reported in J. Matthee et al. (2024). To explain the line profile of J1148-18404 in our model, a substantially high covering fraction ($C \gtrsim 0.8$) is needed. Along with the slightly redshifted center ($\Delta v \simeq +\ 50\,{\rm km\,s}^{-1}$), the absorption may trace dense inflowing gas into the nucleus.

Figure 5 illustrates how the spectral shape changes with different widths of the absorption feature, varying b from 50 to $400\,{\rm km\,s}^{-1}$. For the case of $b = 50\,{\rm km\,s}^{-1}$, the absorption feature is narrow and thus can be resolved with a spectral resolution of $R \gtrsim 1500$ (medium resolution). As the width increases and approaches the velocity shift ($\Delta v = -200\,{\rm km\,s}^{-1}$), absorption begins to affect the redder side of the emission line. In the most extreme case, where the absorption width is significantly large, the absorption profile becomes saturated, and box-shaped troughs are imprinted on both the blue and red side of the narrow-line emission.

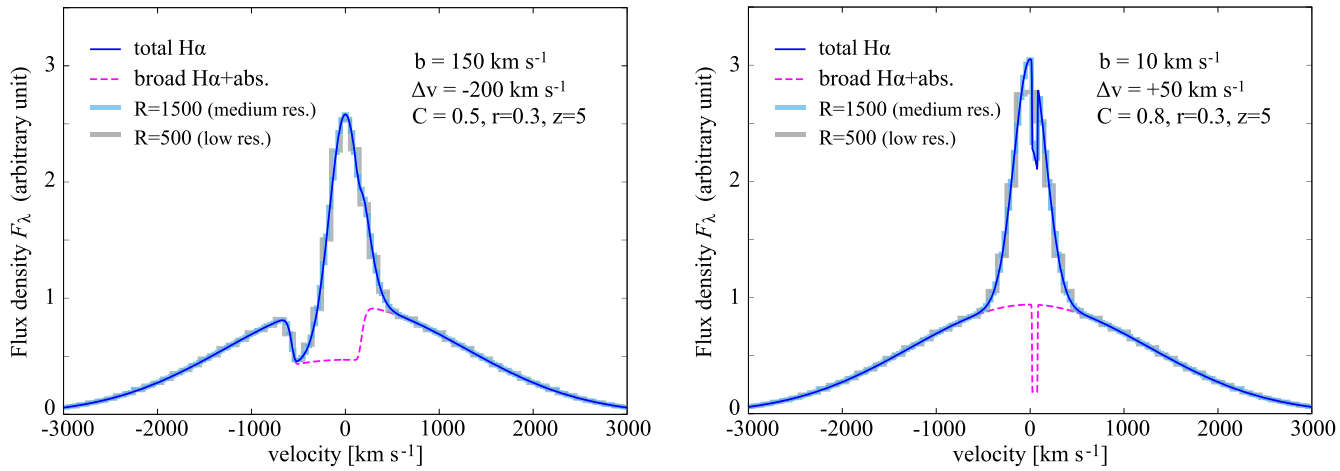

Figure 4. The Hα line profiles with $\mathrm{FWHM_{broad}} = 3000\,\mathrm{km\,s^{-1}}$, $\mathrm{FWHM_{narrow}} = 400\,\mathrm{km\,s^{-1}}$, and $r = 0.3$. We explore two cases: $b = 150\,\mathrm{km\,s^{-1}}$, $\Delta v = -200\,\mathrm{km\,s^{-1}}$, and $C = 0.5$ (left panel) and $b = 10\,\mathrm{km\,s^{-1}}$, $\Delta v = +50\,\mathrm{km\,s^{-1}}$, and $C = 0.8$ (right panel). The solid and dashed curves show the total Hα line profile and the broad component with absorption by dense gas clumps with a column density of $n = 2$ atomic hydrogen, $N_{\mathrm{H},n=2} = 10^{16}\,\mathrm{cm^{-2}}$. The total line profile with a finite spectral resolution ($R \equiv \Delta\lambda/\lambda_0 = 1500$ and 500) is overlaid, where the source redshift is set to $z = 5$.

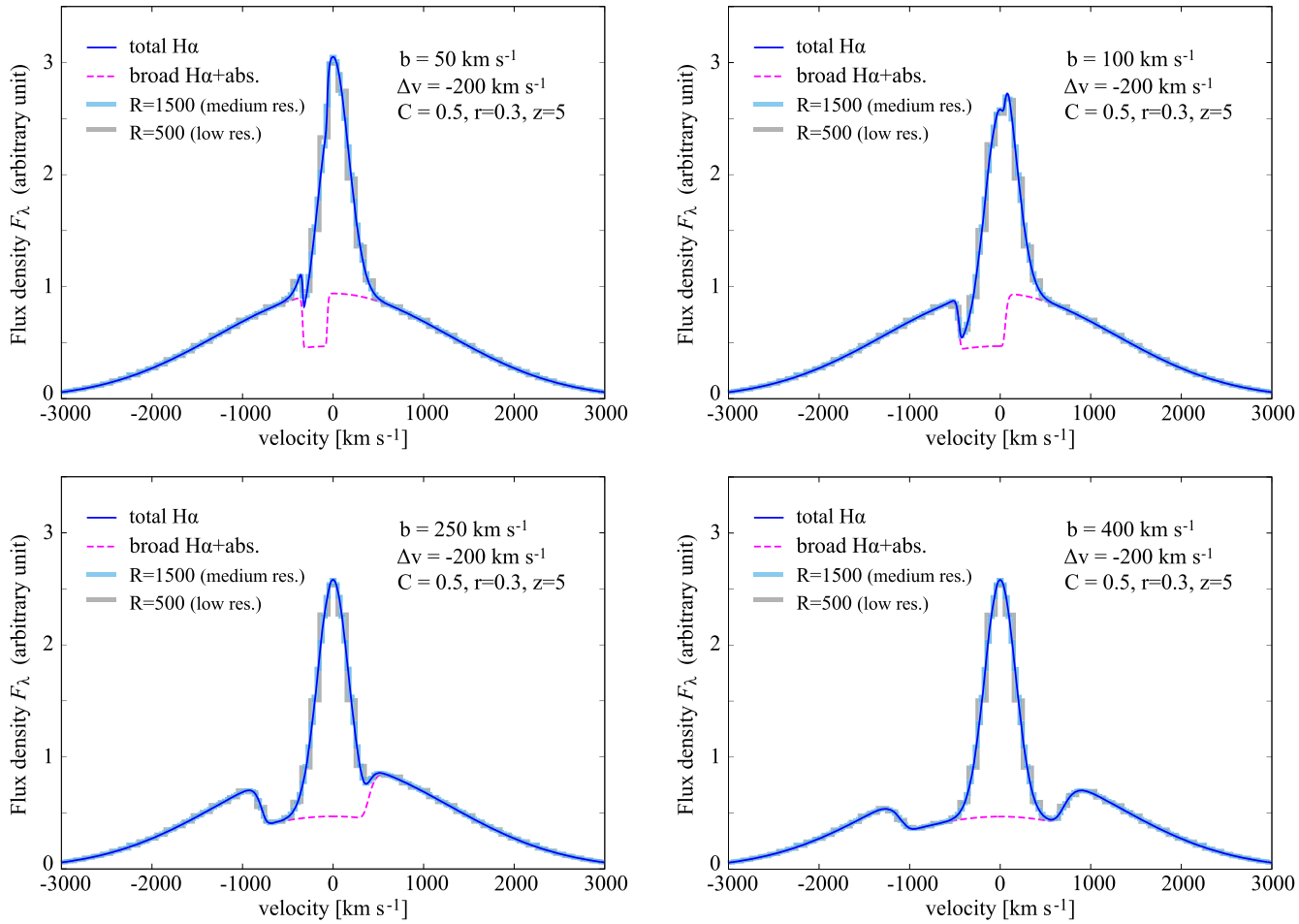

Figure 5. Same as in Figure 4 but illustrating how the line shape changes with the width of the absorption feature, varying b from 50 to 400 $\mathrm{km\,s^{-1}}$. The other parameters are identical to those used in Figure 4.

4. Discussion

4.1. Inflow, Outflow, and BH Feeding Rates

Using the properties of dense gas clumps measured from spectral line analyses, one can estimate the mass inflow, outflow, and BH feeding rate. The detection of Balmer absorption blueshifted by $\Delta v \sim$ a few $\times\ 100\,\mathrm{km\,s^{-1}}$ suggests the presence of dense neutral outflows in the nucleus. Estimating the maximum outflow velocity as $v_{\mathrm{out}} = |\Delta v| + 2\sigma_v \simeq 2|\Delta v|$, the outflow condition yields

$v_{\rm out} \gtrsim \sqrt{2GM_\bullet/R}$, where R is the distance of the dense gas from the central BH with a mass of $M_\bullet$,

$$R \sim \frac{GM_\bullet}{2(\Delta v)^2} \simeq 0.5 \quad {\rm pc} \quad M_7 \Delta v_{200}^{-2}, \tag{7}$$

where $\Delta v_{200} = \Delta v/(200\,{\rm km\,s^{-1}})$ and $M_7 = M_\bullet/(10^7\,M_\odot)$. We note that this distance estimate agrees with that derived from $\log U = -1.5$ (see Section 2), assuming $n_{\rm H} = 3 \times 10^9\,{\rm cm^{-3}}$ and the bolometric luminosity to be the Eddington value for $M_7 = 1$.

The mass outflow rate is calculated by

$$\dot{M}_{\rm out} = 4\pi C \mu m_{\rm p} N_{\rm H} R v_{\rm out} \sim 1.2 \quad M_\odot\ {\rm yr^{-1}} M_7 |\Delta v_{200}|^{-1}, \tag{8}$$

where $\mu = 1.22$ is the mean molecular weight and $N_{\rm H} = 5 \times 10^{22}\,{\rm cm^{-2}}$ and $C = 1$ are set.[6] This outflow rate is $\simeq$5 times higher than the Eddington accretion rate, $\dot{M}_{\rm Edd} \equiv 0.23 M_7 \quad M_\odot\ {\rm yr^{-1}}$. The ratio of $\dot{m}_{\rm out} \equiv \dot{M}_{\rm out}/\dot{M}_{\rm Edd} \simeq 5$ is independent of the BH mass. In a steady state, mass conservation gives the BH feeding rate as $\dot{M}_\bullet = \dot{M}_{\rm in} - \dot{M}_{\rm out} (\geqslant 0)$. When the gas supplying rate from larger radii exceeds the Eddington rate, i.e., $\dot{m}_{\rm in} \equiv \dot{M}_{\rm in}/\dot{M}_{\rm Edd} > 1$, radiation-driven outflows carry the inflowing mass away and decrease the BH feeding rate from the original inflow rate (e.g., Y.-F. Jiang et al. 2014; F. Yuan & R. Narayan 2014). Adopting a mechanical feedback model obtained in radiation hydrodynamic simulations of gas accretion at a vicinity of a BH, the BH feeding rate is given by a scaling relationship of $\dot{m}_\bullet \simeq \dot{m}_{\rm in}^{1/2}$ (H. Hu et al. 2022). Given the formula, the inflow and BH feeding rates can be derived as

$$\dot{m}_{\rm in} = \frac{1 + 2\dot{m}_{\rm out} + \sqrt{1 + 4\dot{m}_{\rm out}}}{2} \simeq 7.8,$$
$$\dot{m}_\bullet = \frac{1 + \sqrt{1 + 4\dot{m}_{\rm out}}}{2} \simeq 2.8 \tag{9}$$

for $\dot{m}_{\rm out} \simeq 5$. Thus, the BH in this system grows in mass at a moderately super-Eddington rate.

4.2. Radiative Signatures of Rapidly Growing BHs Embedded in Dense Environments

We have shown that dense circumnuclear gas can produce a Balmer break in the AGN continuum spectrum and cause absorption in the Hα and Hβ emission line. Here, we discuss additional features of the spectrum under these circumstances. In conditions of $n_{\rm H} \gtrsim 10^{9-10}\,{\rm cm^{-3}}$, where H$\alpha$ absorption ($n = 2 \rightarrow 3$) arises from hydrogen gas in the first-excited $n = 2$ states, the Lyβ-line transition ($n = 3 \rightarrow 1$) also occurs frequently, but these photons are effectively trapped within such a dense medium. Resonance fluorescence by Lyβ leads to excitation of neutral oxygen and produces three O I emission lines (λ1304, λ8446, and λ11287), owing to a coincidence of energy levels between neutral oxygen and hydrogen (J. Kwan & J. H. Krolik 1981). Indeed, these O I lines are observed in low-redshift AGNs as a proxy of dense circumnuclear regions (e.g., S. A. Grandi 1980; M. L. Martínez-Aldama et al. 2015; V. Cracco et al. 2016) and show good correlations with the properties of other low-ionization lines, such as Ca II and Fe II, which originate from the same portion of BLR clouds (A. Rodríguez-Ardila et al. 2002a; R. Riffel et al. 2006; Y. Matsuoka et al. 2007, 2008). The usefulness of these O I emission lines has been noted in K. Inayoshi et al. (2022b), who studied the accretion process of seed BHs in early, metal-poor protogalaxies by performing radiation hydrodynamic simulations. Their work has claimed that JWST NIRSpec observations of low-ionization O I emission lines can test whether the BH is fed via a dense accretion disk at super-Eddington rates.

Intriguingly, two of the O I emission lines (λ8446 and λ11287) have been detected in some JWST-identified AGNs: GN-28074 at $z_{\rm spec} = 2.26$ (I. Juodžbalis et al. 2024) and RUBIES-BLAGN-1 at $z_{\rm spec} = 3.1$ (B. Wang et al. 2024a).[7] For GN-28074, the flux ratio of the O I emission lines is close to unity, indicating that they are likely produced by Lyβ fluorescence. However, constraints on the O I λ1304 line are required to establish the Lyβ pumping scenario in a robust way (A. Rodríguez-Ardila et al. 2002b), while this line is not covered by the wavelength range of the NIRSpec spectrum of GN-28074. Despite the difficulty of confirmation, the Lyβ fluorescence scenario is consistent with the presence of dense gas optically thick to Balmer lines and photons with shorter wavelengths from the Balmer limit. Similarly, B. Wang et al. (2024a) also reported the spectrum of an AGN that exhibits both O I λ8446 and λ11287 lines, though detailed analysis has not been performed for the O I lines.

Another radiative signature of rapidly accreting BHs is a prominent Hα emission line with a large equivalent width (EW), which is predicted to be ${\rm EW_{H\alpha,0}} \simeq 500$–$1500$ Å due to efficient collisional excitation to $n = 3$ states in a dense super-Eddington accretion disk (K. Inayoshi et al. 2022b). This prediction aligns with observations of JWST-identified AGNs at $z > 4$, which typically show EWs approximately 3 times higher than those of quasars at lower redshifts of $z < 0.6$ (R. Maiolino et al. 2024a). The higher EW suggests that the JWST AGN population is embedded by dense gas with a high covering fraction, enhancing the reprocess efficiency of Hα emission. In addition, super-Eddington accreting (seed) BHs at $z \gtrsim 8$ are expected to be detectable through a unique color excess in the JWST NIRCam/MIRI bands the redshifted Hα line enters (K. Inayoshi et al. 2022b). A larger samples of broad-Hα emitters will bring insights into the properties of JWST-identified AGNs (e.g., Hα EWs, Eddington ratios, and BH masses; see a recent work by X. Lin et al. 2024).

4.3. Steepness and Depth of a Balmer Break

In our model, where JWST AGNs are embedded in very dense gas clumps, the Balmer break-like spectral features observed in some LRDs are attributed to absorption at wavelengths shorter than the Balmer limit by these dense gas clouds. However, the discontinuity in the spectrum near the Balmer limit, as shown in Figure 1, appears more abrupt than what is observed in the PRISM data for these LRDs. This difference arises because our model employs a simplified

[6] We consider a continuous density distribution with some degree of clumpiness in the outflowing region rather than a single thin-shell structure. Such profiles arise from continuous mass loading by disk winds, as predicted by numerical simulations (K. Ohsuga et al. 2009; F. Yuan & R. Narayan 2014; H. Hu et al. 2022). Regardless of the origin of the cloud clumpiness, the column density can be determined as $N_{\rm H} \simeq n_{\rm H}(R)R$. Given a column density, the degree of clumpiness can be adjusted by increasing the density $n_{\rm H}$ while decreasing the slab thickness Δs (see Section 2).

[7] GN-28074 shows clear blueshifted absorption features on the Hα, Hβ, and He I λ10830 emission lines (I. Juodžbalis et al. 2024). RUBIES-BLAGN-1 exhibits a strong blueshifted absorption feature in He I λ10830 within a wavelength coverage of the G395M spectra. However, the presence of the Balmer absorption in this object remains unclear because of the lower spectral resolution of the PRISM data (B. Wang et al. 2024a).

absorber with a uniform density and nonturbulent slab, leading to a nearly isothermal temperature structure ($T \simeq 8000$–10^4 K). For comparison, individual stellar spectra with surface temperatures of $\simeq$8000–10^4 K show a profound and steep Balmer break (R. L. Kurucz 1979; B. M. Poggianti & G. Barbaro 1997). In contrast, spectra near the Balmer limit in cooler, lower-mass stars are substantially smoother, creating a gradual Balmer break in galaxies where long-lived, low-mass stars dominate the light (e.g., G. Worthey 1994). By this analogy, a smooth Balmer break could also be produced in our model if the density structure of absorbers were nonuniform, turbulent, and multiphased (e.g., K. Wada et al. 2016), including cooler region. Indeed, X. Ji et al. (2025) find that microscopic turbulence makes the Balmer break feature smoother, better matching the spectral shapes observed in some LRDs. While a detailed analysis of these effects is beyond the scope of our work, future observations that measure the continuum shapes of JWST AGNs in larger samples could potentially constrain the density and temperature structure of the absorbing gas.

Moreover, the depth of the Balmer break in our model depends on the hydrogen column density of gas absorbers. For the six LRDs shown in Figure 3, the narrow range of Balmer break strengths ($\sim$2–2.5) indicates the need for a specific column density. However, this narrow range might also reflect a photometric selection bias as LRDs are typically identified with a consistent reddening level ($A_V \simeq 3$ mag). The column density conditions naturally produce Balmer break strengths within the observed range ($\sim$eq 2–3).

In contrast, the stellar-origin scenario explains the Balmer break feature through stellar populations of specific ages (several hundred megayears; see Figure A1 in B. Wang et al. 2024b). Although these models predict an upper limit for the Balmer break strength of $\lesssim$2.5, marginally consistent with the brightest LRD (A2744-45924; I. Labbe et al. 2024), fine-tuning of stellar ages and populations are required to match the observations. To differentiate these scenarios, discovering a deeper Balmer break feature that cannot be reproduced by stellar-origin models would provide decisive evidence supporting the AGN-origin scenario.

4.4. Implications of Stellar Populations in LRDs and Ultramassive Quiescent Galaxies at High Redshifts

Thus far, we have observed several LRDs that show continuum spectra with a Balmer break. If these LRDs are powered by starbursts alone, an extremely massive stellar mass comparable to that of the Milky Way ($M_\star \sim 10^{11}\,M_\odot$) would be derived (J. F. W. Baggen et al. 2024; L. J. Furtak et al. 2024; B. Wang et al. 2024b). Considering their high abundance within a cosmic volume ($\sim 10^{-5}\,\mathrm{Mpc}^{-3}$), the inferred stellar mass density would exceed the theoretical upper bound in a flat Lambda cold-dark-matter (CDM) universe, with a 100% baryon-to-star conversion factor or $\gtrsim$10%–20% (B. Wang et al. 2024b; H. B. Akins et al. 2024). Additionally, in this stellar-origin hypothesis, the very compact nature of LRDs suggests the presence of unrealistically dense stellar clusters in these LRDs, with surface density above $\gtrsim 10^6 M_\odot\,\mathrm{pc}^{-2}$ (e.g., J. F. W. Baggen et al. 2024), which is 1 order of magnitude higher than the densest star clusters or the densest elliptical galaxy progenitors (P. F. Hopkins et al. 2010; J. F. W. Baggen et al. 2023). If this scenario is true, a large number ($\gg 10\,\mathrm{yr}^{-1}$) of tidal disruption events (TDEs) would be observed even within a small area ($\lesssim 0.1\,\mathrm{deg}^2$) of deep JWST surveys (K. Inayoshi et al. 2024).[8]

In contrast, under the scenario where the Balmer break is caused by gas absorption surrounding the AGN, the stellar mass inferred from SED fitting can be dramatically reduced, thereby resolving the tension with the ΛCDM framework. This interpretation also aligns with the observation that LRDs are extremely compact, possibly dominated by an unresolved source in most cases. Moreover, this supports an idea that the BH population at the early epochs tends to be overmassive relative to the mass correlation, with its host mass observed in the local universe (e.g., Y. Harikane et al. 2023; R. Maiolino et al. 2024), as suggested by numerical simulations that sufficiently resolve the galactic nuclear scales at $\lesssim$0.1–1 pc (e.g., K. Inayoshi et al. 2022a, 2022b).

Additionally, recent JWST observations have revealed very massive quiescent galaxies in the distant universe that have already quenched star formation at $z > 6$ (A. C. Carnall et al. 2023, 2024; A. de Graaff et al. 2024; A. Weibel et al. 2024). Some of these galaxies also show broad Hα emission, indicating the presence of AGNs (and in others the presence of an AGN cannot be easily excluded). Similar to LRDs, these massive galaxies face the same issue of exceeding the ΛCDM stellar mass density limit. However, if the Balmer break and absorption features in their spectra are partly due to dense gas absorption, and their continua are contributed by an AGN, this could help alleviate some of the inferred cosmological tensions.

4.5. He I Absorption and Emission

Similar to Balmer lines, a blueshifted absorption feature is also observed in the He I λ10830 emission line for the two JWST-identified AGNs, which simultaneously show Balmer absorption (I. Juodžbalis et al. 2024; B. Wang et al. 2024a; see the discussion in Section 4.2). For the two objects, the velocity shift tends to be larger than that of the Balmer lines. This absorption is caused by the metastable triplet state 2^3S (or $1s2s^3S_1$) for helium with a column density of $N_{\mathrm{He}}(2^3S) \sim (1\text{–}3) \times 10^{14}\,\mathrm{cm}^{-2}$. Based on photoionization models, He I absorption features consistent with the observations can be reproduced under the conditions where Balmer absorption becomes prominent (I. Juodžbalis et al. 2024).

We also note that collisional excitation from the metastable 2^3S state to higher excitation levels can enhance the intensity of three emission lines of He I λ3890, λ5877, and λ7067 (corresponding to transitions from the $1s3s$, $1s3p$, and $1s3d$ states of triplet helium to the lower-energy states; see Figure 14.3 and Table 14.5 of B. T. Draine 2011). The latter two emission lines are indeed observed in the spectra of the two sources mentioned above, although detailed analyses have not been conducted for the He I emission lines (see Figure 2 of B. Wang et al. 2024a and Figure 1 of I. Juodžbalis et al. 2024). Further explorations of the extremely dense interstellar medium within high-redshift AGNs, particularly those identified through JWST observations, will provide deeper insights into the physics of early BH assembly.

[8] K. Inayoshi et al. (2024) estimated the stellar mass density as $\sim 5 \times 10^4 M_\odot\,\mathrm{pc}^{-2}$ based on the dust mass required to achieve an extinction level of $A_V \simeq 3$ mag, which explains the red continua observed in LRDs. Thus, the predicted TDE detection number is as low as $\sim$2–10 and 0.2–2 yr^{-1} for JADES-Medium and COSMOS-Web, respectively.

Acknowledgments

We greatly thank Yuhiko Aoyama, Seiji Fujimoto, Jenny Greene, Kevin Hainline, Jakob Helton, Luis C. Ho, Harley Katz, Kei Tanaka, and Bingjie Wang for the constructive discussions. K.I. acknowledges support from the National Natural Science Foundation of China (12073003, 11721303, 11991052) and the China Manned Space Project (CMS-CSST-2021-A04 and CMS-CSST-2021-A06). R.M. acknowledges support by the UKRI Frontier Research grant RISEandFALL and from a research professorship from the Royal Society. This research was supported in part by grant NSF PHY-2309135 to the Kavli Institute for Theoretical Physics (KITP). We are deeply grateful to Raffaella Schneider, Rachel Somerville, Brant Robertson, and Volker Bromm for organizing the KITP workshop, "Cosmic Origins: The First Billion Years," which provided the initial inspiration for this research.

ORCID iDs

Kohei Inayoshi https://orcid.org/0000-0001-9840-4959
Roberto Maiolino https://orcid.org/0000-0002-4985-3819

References

Akins, H. B., Casey, C. M., Lambrides, E., et al. 2024, arXiv:2406.10341
Baggen, J. F. W., van Dokkum, P., Brammer, G., et al. 2024, ApJL, 977, L13
Baggen, J. F. W., van Dokkum, P., Labbé, I., et al. 2023, ApJL, 955, L12
Barro, G., Pérez-González, P. G., Kocevski, D. D., et al. 2024, ApJ, 963, 128
Baskin, A., & Laor, A. 2018, MNRAS, 474, 1970
Carnall, A. C., Cullen, F., McLure, R. J., et al. 2024, MNRAS, 534, 325
Carnall, A. C., McLure, R. J., Dunlop, J. S., et al. 2023, Natur, 619, 716
Cracco, V., Ciroi, S., Berton, M., et al. 2016, MNRAS, 462, 1256
de Graaff, A., Setton, D. J., Brammer, G., et al. 2024, NatAs, Advanced Online Publication
Draine, B. T. 2011, Physics of the Interstellar and Intergalactic Medium (Princeton, NJ: Princeton Univ. Press),
Drawin, H. W. 1969, ZPhy, 225, 483
Ferland, G. J., Chatzikos, M., Guzmán, F., et al. 2017, RMxAA, 53, 385
Furtak, L. J., Labbé, I., Zitrin, A., et al. 2024, Natur, 628, 57
Grandi, S. A. 1980, ApJ, 238, 10
Greene, J. E., Labbe, I., Goulding, A. D., et al. 2024, ApJ, 964, 39
Harikane, Y., Zhang, Y., Nakajima, K., et al. 2023, ApJ, 959, 39
Hopkins, P. F., Murray, N., Quataert, E., & Thompson, T. A. 2010, MNRAS, 401, L19
Hu, H., Inayoshi, K., Haiman, Z., Quataert, E., & Kuiper, R. 2022, ApJ, 934, 132
Inayoshi, K., & Ichikawa, K. 2024, ApJ, 973, L49
Inayoshi, K., Kashiyama, K., Li, W., et al. 2024, ApJ, 966, 164
Inayoshi, K., Nakatani, R., Toyouchi, D., et al. 2022a, ApJ, 927, 237
Inayoshi, K., Onoue, M., Sugahara, Y., Inoue, A. K., & Ho, L. C. 2022b, ApJL, 931, L25
Ji, X., Maiolino, M., Sugahara, R., Übler, A. K., et al. 2025, arXiv:2501.13082
Jiang, Y.-F., Stone, J. M., & Davis, S. W. 2014, ApJ, 796, 106
Juodžbalis, I., Ji, X., Maiolino, R., et al. 2024, MNRAS, 535, 853
Kocevski, D. D., Finkelstein, S. L., Barro, G., et al. 2024, arXiv:2404.03576
Kocevski, D. D., Onoue, M., Inayoshi, K., et al. 2023, ApJL, 954, L4
Kokorev, V., Caputi, K. I., Greene, J. E., et al. 2024a, ApJ, 968, 38
Kokorev, V., Chisholm, J., Endsley, R., et al. 2024b, ApJ, 975, 178
Kurucz, R. L. 1979, ApJS, 40, 1
Kwan, J., & Krolik, J. H. 1981, ApJ, 250, 478
Labbe, I., Greene, J. E., Bezanson, R., et al. 2023, arXiv:2306.07320
Labbe, I., Greene, J. E., Matthee, J., et al. 2024, arXiv:2412.04557
Li, Z., Inayoshi, K., Chen, K., Ichikawa, K., & Ho, L. C. 2025, ApJ, 980, 36
Lin, X., Wang, F., Fan, X., et al. 2024, ApJ, 974, 147
Maiolino, R., Risaliti, G., Signorini, M., et al. 2024a, arXiv:2405.00504
Maiolino, R., Scholtz, J., Curtis-Lake, E., et al. 2024, A&A, 691, A145
Maiolino, R., Scholtz, J., Witstok, J., et al. 2024b, Natur, 627, 59
Martínez-Aldama, M. L., Dultzin, D., Marziani, P., et al. 2015, ApJS, 217, 3
Matsuoka, Y., Kawara, K., & Oyabu, S. 2008, ApJ, 673, 62
Matsuoka, Y., Oyabu, S., Tsuzuki, Y., & Kawara, K. 2007, ApJ, 663, 781
Matthee, J., Naidu, R. P., Brammer, G., et al. 2024, ApJ, 963, 129
Novikov, I. D., & Thorne, K. S. 1973, in Black Holes (Les Astres Occlus), ed. C. DeWitt & B. DeWitt (New York: Gordon and Breach), 343
Ohsuga, K., Mineshige, S., Mori, M., & Kato, Y. 2009, PASJ, 61, L7
Onoue, M., Inayoshi, K., Ding, X., et al. 2023, ApJL, 942, L17
Poggianti, B. M., & Barbaro, G. 1997, A&A, 325, 1025
Riffel, R., Rodríguez-Ardila, A., & Pastoriza, M. G. 2006, A&A, 457, 61
Rodríguez-Ardila, A., Viegas, S. M., Pastoriza, M. G., & Prato, L. 2002a, ApJ, 565, 140
Rodríguez-Ardila, A., Viegas, S. M., Pastoriza, M. G., Prato, L., & Donzelli, C. J. 2002b, ApJ, 572, 94
Tanaka, K. E. I., & Omukai, K. 2014, MNRAS, 439, 1884
Vanden Berk, D. E., Richards, G. T., Bauer, A., et al. 2001, AJ, 122, 549
Wada, K., Schartmann, M., & Meijerink, R. 2016, ApJL, 828, L19
Wang, B., de Graaff, A., Davies, R. L., et al. 2024a, arXiv:2403.02304
Wang, B., Leja, J., de Graaff, A., et al. 2024b, ApJL, 969, L13
Weibel, A., de Graaff, A., Setton, D. J., et al. 2024, arXiv:2409.03829
Worthey, G. 1994, ApJS, 95, 107
Yuan, F., & Narayan, R. 2014, ARA&A, 52, 529
Zappacosta, L., Piconcelli, E., Fiore, F., et al. 2023, A&A, 678, A201